Journal of Zhejiang University-SCIENCE A (Applied Physics & Engineering)
ISSN 1673-565X (Print); ISSN 1862-1775 (Online)
www.jzus.zju.edu.cn; www.springerlink.com
E-mail: jzus@zju.edu.cn

Experimental study and analysis of shock train self-excited oscillation in an isolator with background waves*

Wen-xin HOU[1], Jun-tao CHANG[†‡1], Chen KONG[1], Wen BAO[1], Laurent DALA[2]

[1]*School of Energy Science and Engineering, Harbin Institute of Technology, Harbin 150001, China*

[2]*Department of Mechanical and Construction Engineering, Northumbria University, Newcastle upon Tyne, NE1 8ST, UK*

[†]E-mail: changjuntao@hit.edu.cn

Received Feb. 5, 2019; Revision accepted July 15, 2020; Crosschecked Aug. 6, 2020

Abstract: A study of shock train self-excited oscillation in an isolator with background waves was implemented through a wind tunnel experiment. Dynamic pressure data were captured by high-frequency pressure measurements and the flow field was recorded by the high-speed Schlieren technique. The shock train structure was mostly asymmetrical during self-excited oscillation, regardless of its oscillation mode. We found that the pressure discontinuity caused by background waves was responsible for the asymmetry. On the wall where the pressure at the leading edge of the shock train was lower, a large separation region formed and the shock train deflected toward to the other wall. The oscillation mode of the shock train was related to the change of wall pressure in the oscillation range of its leading edge. The oscillation range and oscillation intensity of the shock train leading edge were affected by the wall pressure gradient induced by background waves. When located in a negative pressure gradient region, the oscillation of the leading edge strengthened; when located in a positive pressure gradient region, the oscillation weakened. To find out the cause of self-excited oscillation, correlation and phase analyses were performed. The results indicated that the instability of the separation region induced by the leading shock was the source of perturbation that caused self-excited oscillation, regardless of the oscillation mode of the shock train.

Key words: Self-excited oscillation; Background waves; Asymmetrical structure; Source of perturbation
https://doi.org/10.1631/jzus.A2000042 **CLC number:** V231.3

1 Introduction

Hypersonic vehicles have attracted much attention from researchers in recent decades, and scramjet is considered to be the optimal propulsion system for hypersonic flight (Liao et al., 2018; Wen et al., 2019; Zhang et al., 2019). As an important component of a scramjet, the isolator compresses the high velocity airflow and blocks mutual interference between the inlet and the combustion chamber (Xing et al., 2017). The airflow compression in the isolator is achieved by a series of shock waves, also known as a shock train. The structure and behavior of the shock train directly affect the airflow parameters at the outlet of the isolator, thereby affecting the combustion. Moreover, if the shock train is pushed out of the isolator due to excessive backpressure, inlet unstart occurs and engine performance deteriorates sharply (Jiao et al., 2016). Therefore, understanding the characteristics of the shock train is helpful to maintain the stable and efficient operation of the engine. Steady-state shock trains have been studied for decades. Many parameters of the upstream flow affect the structure and length of the shock train. These include the Mach number (Waltrup and Billig, 1973; Sugiyama et al., 2008), boundary layer thickness (Fiévet et al., 2017), and velocity distribution (Tam et al., 2013). The

‡ Corresponding author
* Project supported by the National Natural Science Foundation of China (Nos. 11972139 and 51676204)
ORCID: Wen-xin HOU, https://orcid.org/0000-0002-1322-4359; Jun-tao CHANG, https://orcid.org/0000-0003-0019-2068

backpressure downstream of the isolator also affects the shock train length and motion (Cai et al., 2017). In addition to the upstream and downstream conditions, the isolator geometry parameters, such as the aspect ratio (Geerts and Yu, 2016) and divergent angle (Huang et al., 2011), are critical to the 3D shock train structure. Matsuo et al. (1999) and Gnani et al. (2016) have summarized previous research on this subject.

In recent years, the unsteady characteristics of shock trains have attracted more attention from researchers (Lu et al., 2018; Wang et al., 2018). Self-excited oscillation is one of the most significant unsteady characteristics. Even when the upstream and downstream conditions of the isolator remain unchanged, shock train oscillations still occur. The oscillation of the shock train is accompanied by fluctuation in the flow parameters at the isolator exit, which feeds instabilities to the combustor. The pressure fluctuations induced by the oscillations not only generate noise affecting the comfort of manned aircraft, but also cause intense fluctuating wall loads resulting in structural fatigue. If the oscillation range is wide enough, the shock train may move upstream of the isolator and into the inlet, causing inlet unstart and performance degradation. Therefore, studies of self-excited oscillations are useful for developing strategies to reduce unsteadiness and increase the operating margin of the engine.

Researchers have worked hard to explain the underlying flow mechanisms of self-excited oscillations. To date, three principal theories have been proposed to explain the cause of unsteadiness. Ikui et al. (1974) experimentally investigated shock train self-excited oscillation and conjectured that the upstream flow perturbations led to the oscillation. Yamane et al. (1984) statistically analyzed the wall pressure measured in the oscillation and considered that self-excited oscillation was caused by a downstream acoustic resonance. Sugiyama et al. (1988) suggested that a change of boundary layer thickness in the vicinity of the leading shock caused the oscillation. An aerodynamic throat is formed between the first and second shocks, and the throat cross section changes with increasing or decreasing boundary layer thickness, which results in the motion of the shock train. The three theories are all different, and researchers have reached no consensus about the mechanism of self-excited oscillation. In addition to research on the mechanism, some studies have focused on the factors influencing the oscillation. Su and Zhang (2013) numerically studied the effect of backpressure on self-excited oscillation. The position and structure of the shock train remained stable when the backpressure was low, but oscillations emerged when the backpressure was high. To suppress the oscillation, they used a periodic jet to manipulate the cowl reflected shock wave (Su et al., 2018). Even when the incoming flow is uniform, the structure of the shock train may be asymmetric. Carroll and Dutton (1990) observed an asymmetric shock train in a Mach 2.45 experiment. The separation zones on the opposing walls showed different flow patterns due to the asymmetric structure. Xiong et al. (2017a) experimentally studied self-excited oscillation in a Mach 3 wind tunnel and also observed an asymmetric shock train. According to the deflection direction of the shock train, two separation modes were summarized and compared. The influence of backpressure was further investigated, and the results showed that the oscillation frequency increased with increasing backpressure (Xiong et al., 2017b). Hunt and Gamba (2018) demonstrated that the internal structure of the shock train changes during oscillation because the oscillation frequencies of shock waves at different positions inside the shock train were different. Until now, most studies of self-excited oscillations have been carried out in a uniform flow. However, the characteristics of self-excited oscillations in an isolator with background waves remain unclear.

The term background waves refer to a series of shock waves and expansion waves existing in an isolator under unthrottled conditions. Background waves are generated when the airflow entering the isolator has been non-uniform after the compression of the inlet. Background waves have a significant influence on shock train motion. Wagner et al. (2009) investigated the unstart process in an inlet-isolator model and discovered that the velocity of the shock train varied greatly during upstream propagation. Tan et al. (2012) experimentally studied the shock train motion in an isolator with background waves. They found that the shock train underwent unstable stages when passing through the impingement point of background shock waves. Xu et al. (2016, 2017) investigated the rapid movement of a shock train and discovered that the wall pressure gradient induced by background waves had an impact on shock train motion. Further experimental results indicated that a

local throat-like shape at the shock train head has a limit value which would trigger rapid movement of the shock train (Xu et al., 2018). Li et al. (2017) constructed a low-order dynamic model to predict the path of a shock train affected by background waves, and analyzed its rapid forward movement using free interaction theory. Different types of background waves have different effects on shock train motion. Li et al. (2018) summarized three types of shock wave distributions in the isolator. The results showed that shock train oscillations affected by different distributions differed in temporal and spatial scales. Shi et al. (2019a) studied the shock train motion affected by variable background waves. They found a hysteresis loop in the path of the shock train leading edge (STLE). The forced oscillation of a shock train in a hypersonic inlet with a translating cowl was investigated by numerical simulation (Shi et al., 2019b). The results showed that the shock train moved upstream accompanied by oscillation, as the cowl moved downstream.

In summary, shock train self-excited oscillation without considering the effect of background waves has been studied by many researchers. However, background waves are ubiquitous in actual isolators, and there have been few studies of their effects on self-excited oscillation. In our previous study on shock train self-excited oscillation influenced by background waves, three oscillation modes were observed, distinguishable by the distribution of the wall pressure standard deviation. Self-excited oscillation affected by background waves was compared with oscillation unaffected by background waves (Hou et al., 2020). However, our previous study did not discuss in detail the underlying fundamental flow mechanism, which is the focus of this study. In this study, experiments were carried out in a wind tunnel to understand the cause of the asymmetrical structure of a shock train, the effect of the wall pressure gradient on self-excited oscillation, and the source of the perturbation that causes self-excited oscillation.

2 Experimental and numerical setup

2.1 Experimental facility and measurement methodology

A direct-connect wind tunnel facility (Fig. 1) was used to conduct experiments in this study. The facility is composed mainly of a supersonic nozzle and an isolator. To supply airflow for experiments, a high pressure gas storage tank was linked upstream of the supersonic nozzle. A pneumatic control valve was used to reduce the air pressure to the desired total pressure. In the current experiment, the stagnation pressure of the incoming flow was 5.25×10^5 Pa, and the stagnation temperature was 294 K. At the nozzle exit, the Mach number of the flow was 2.65 and the unit Reynolds number was 4.8×10^7. The thickness of boundary layer was about 2.2 mm. A wedge was mounted at the nozzle exit to induce an oblique shock wave, which would enter the isolator and form the background waves. The dimensions of the steel isolator were: length 320 mm, width 50 mm, and height 30 mm. A quartz glass window was placed on the isolator side walls for the acquisition of flow field Schlieren images. To produce backpressure in a cold flow, a flap was installed downstream of the isolator. By using a stepper motor to change the flap angle, the degree of throttling could be adjusted to generate different backpressures. The resolution of the flap angle was 0.006°. When the flap angle reached 45°, the isolator was completely closed.

To capture the dynamic pressure in the isolator, 20 transducers were mounted on the isolator walls. The comprehensive precision of each transducer was ±0.25% of the full scale. The locations of the transducers are shown in Fig. 1. The sampling frequency of pressure was 10 kHz. A Z-style Schlieren system was used to display the shock train structure. A high-speed camera with a frame rate of 2500 Hz was used to record the shock train motion. Other details of the test facility can be found in our previous study (Hou et al., 2020).

To estimate the pressure measurement errors during experiments, five unthrottled tests were conducted with the same incoming flow parameters. The pressure standard deviation at transducer i can be calculated as

$$\sigma_{p,i}=\sqrt{\frac{1}{5}\sum_{n=1}^{5}\left(p_{n,i}-\frac{1}{5}\sum_{n=1}^{5}p_{n,i}\right)^2}, \tag{1}$$

where $p_{n,i}$ is the wall pressure at transducer i (i=1, 2, …, 9) in the nth test. The calculated pressure standard deviation is shown in Fig. 2. The maximum pressure standard deviation normalized by the static

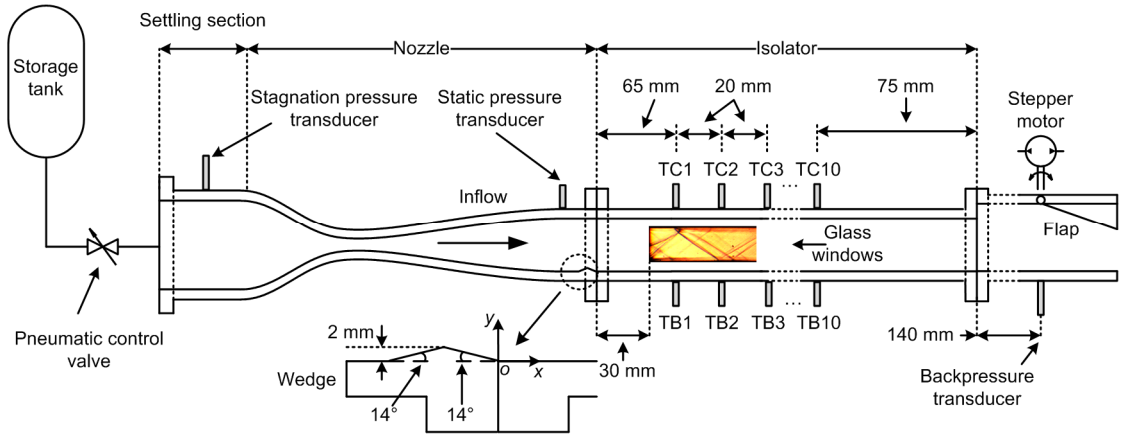

Fig. 1 Schematic diagram of the wind tunnel facility

TC1, TC2, …, TC10: transducers on the top wall; TB1, TB2, …, TB10: transducers on the bottom wall

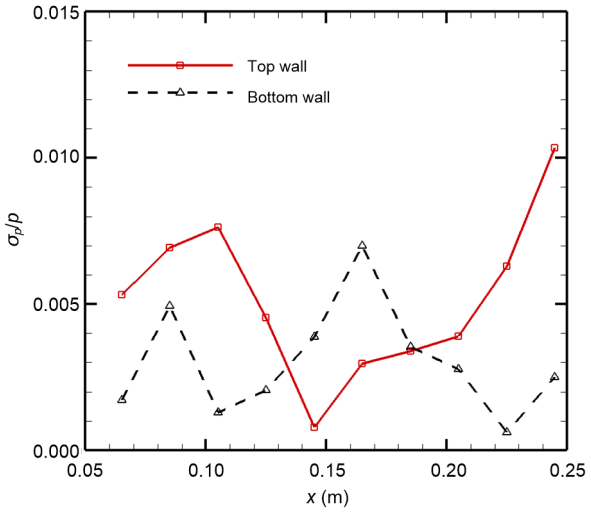

Fig. 2 Standard deviation of wall pressure *p*

pressure of freestream was less than 0.011, so the accuracy of pressure measurement was high. The position of the STLE was obtained by an image processing technique. Since the resolution of a Schlieren image is 0.3 mm/pixel, the accuracy of the position of the STLE was better than 0.3 mm.

2.2 Numerical approach and validation

To obtain more flow field detail, the commercial computational fluid dynamics (CFD) software Fluent was used to solve the Reynolds-averaged Navier-Stokes (RANS) equations. The *k*-*ω* shear stress transport (SST) turbulence model has proved to be effective in predicting negative pressure gradient flows (Raj and Venkatasubbaiah, 2012), and thus was used in this study. The freestream was modelled as a perfect gas, and the gas viscosity was calculated by Sutherland's law. The advection upstream splitting method (AUSM) was selected for convective flux splitting, and the second-order upwind method was applied for discretization of the governing equations.

The commercial software ICEM was used to generate the structured grid for numerical simulation. A sequence of grids was tested, in which the coarse grid, fine grid, and dense grid contained 1.4×10^5 (1400×100), 3.0×10^5 (2000×150), and 8.0×10^5 (4000×200) cells, respectively. To capture the precise structure of the boundary layers and separation zones, all the grids were refined in the near-wall region along the normal direction. The maximum value of $y+$ was below 0.5 for the wall flow region. Fig. 3 shows the boundary conditions of the test model and part of the dense grid. The accumulated errors during numerical simulations were estimated using the method proposed by Smirnov et al. (2014, 2015). The results are listed in Table 1. The accumulated errors in all simulations were small and the accuracy was high. The wall pressure distributions obtained from numerical simulations are compared with the experimental data in Fig. 4. The results of simulations with different sized grids are almost identical. Only the pressure distribution in the vicinity of the shock reflection points shows slight differences. The numerical results show good agreement with the experimental results. To provide a clear structure of the flow field, the simulation results from the dense grid were selected in this study.

Table 1 Estimates of numerical calculation error

Allowable error	Grid resolution	Number of steps, n_{cal}	Accumulated error	Allowable number of steps, n_{max}	Reliability, n_{max}/n_{cal}
5%	1400×100	80 000	1.0004×10^{-6}	2.4982×10^{9}	3.1227×10^{4}
5%	2000×150	80 000	2.9642×10^{-7}	2.8453×10^{10}	3.5566×10^{5}
5%	4000×200	80 000	1.2502×10^{-7}	1.5996×10^{11}	1.9995×10^{6}

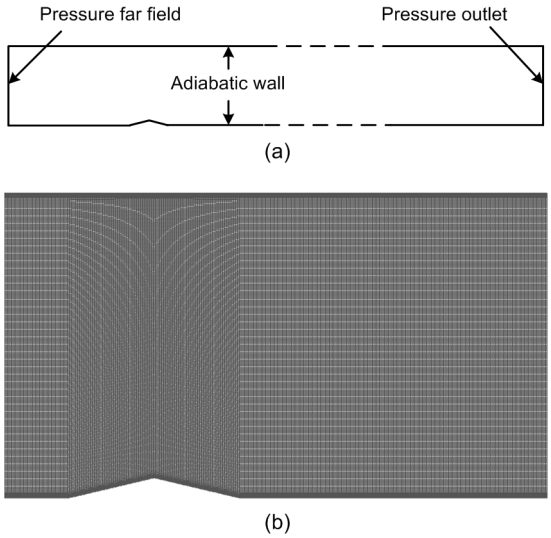

Fig. 3 Boundary conditions of the test model (a) and partial grids (b)

3 Results and discussion

3.1 Background waves in the isolator

The background waves in the isolator, caused by the wedge installed before the isolator entrance (Hou et al., 2020), are shown in Fig. 5. The incident shock induced by the wedge impinges on the top wall of the isolator, generating a separation bubble and a reflected shock. This reflected shock and the reattachment shock generated at the end of wedge enter the optical window of flow field, and reflect between the top wall and bottom wall. A series of shock reflection points are generated, marked as T1, T2, T3, and T4 on the top wall and B1, B2, and B3 on the bottom wall. The wall pressure distributions obtained from numerical simulation are shown in Fig. 6. Since the distribution of background waves is asymmetrical, the pressure distributions on the top wall and bottom wall are different. In the vicinity of the shock reflection points, negative pressure gradient regions are formed. Between the negative pressure gradient regions, positive pressure gradient regions are formed.

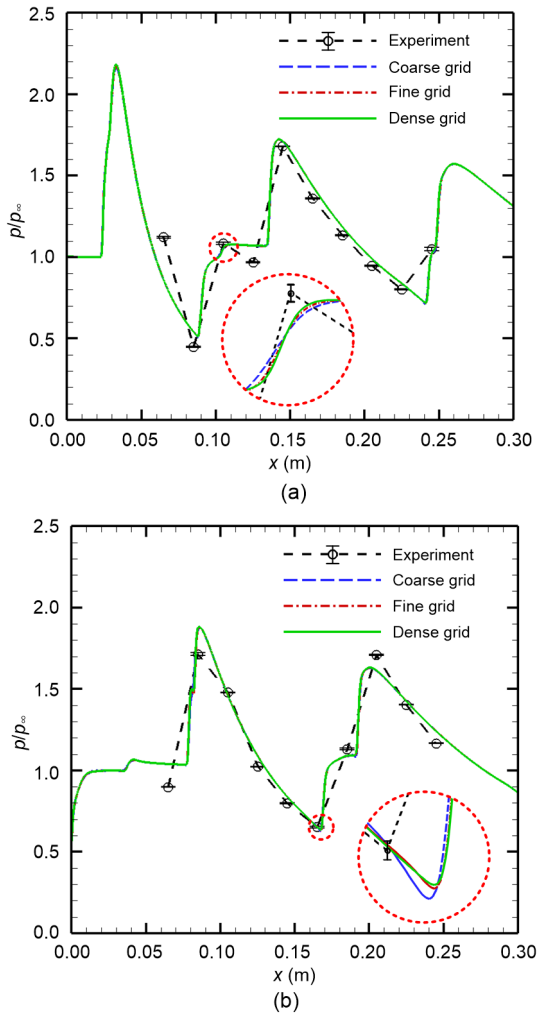

Fig. 4 Comparison of numerical and experimental results
(a) Top wall; (b) Bottom wall. p_∞ indicates the static pressure of freestream

3.2 Cause of the asymmetrical structure of the shock train

The flow field in throttled condition is shown in Fig. 7. At the exit of the isolator, high backpressure is generated due to the throttling effect. A shock train emerges to match the backpressure. The positions of the STLEs on the top wall and bottom wall are marked with white circles in Fig. 7. Obviously, their

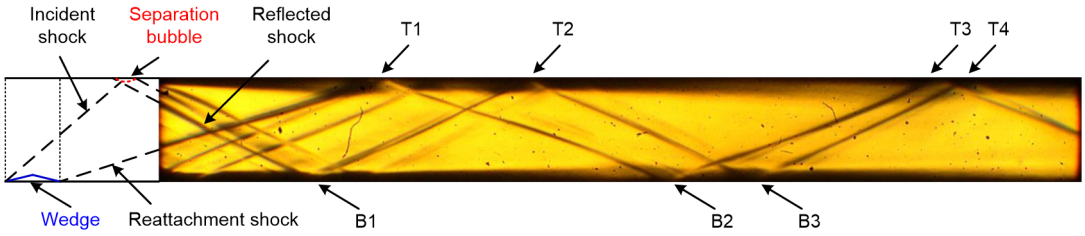

Fig. 5 Background waves in the isolator

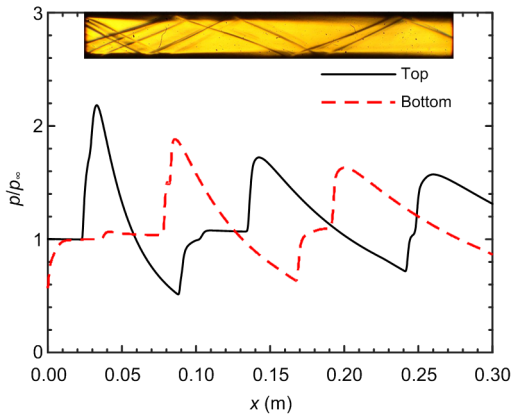

Fig. 6 Wall pressure distributions in unthrottled condition

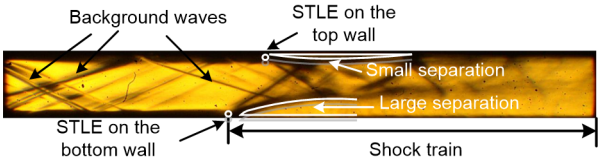

Fig. 7 Schlieren image in throttled condition

streamwise positions are different. In the shock train head region, a large separation region is formed on the bottom wall and a small separation region on the top wall. In the upstream region of the shock train, the flow field is not affected by the backpressure, and thus the background waves are the same as those shown in Fig. 5.

To describe the degree of throttling, the throttling ratio (TR) can be defined as

$$\mathrm{TR}=\frac{A_{\mathrm{th}}}{A_{\mathrm{duct}}}, \tag{2}$$

where A_{th} is the throttling area caused by the flap, and A_{duct} is the cross area of the isolator. When the throttling ratio at the isolator exit remains constant, the shock train undergoes unsteady movement due to self-excited oscillation. However, the structures and mean positions of the shock train during self-excited oscillation are different when the throttling ratio is different. In our previous study on shock train self-excited oscillation influenced by background waves, three different oscillation modes were found (Hou et al., 2020). The histories of the flap angle and corresponding throttling ratio are shown in Fig. 8. The changes in structure of the shock train in different oscillation modes are presented in Fig. 9. When the shock train is in top-large-separation (TLS) mode or bottom-large-separation (BLS) mode, a large separation region is formed on one wall and a small separation region on the other wall. The shock train deflects toward the wall where the small separation region lies. The position of the large separation zone does not change during oscillation. When the shock train is in transition mode, the positions of the large separation region and small separation region change during oscillation. The deflection direction of the shock train varies. In general, during self-excited oscillation, the structure of the shock train is mostly asymmetrical, and the deflection directions of the shock train are different in different oscillation modes.

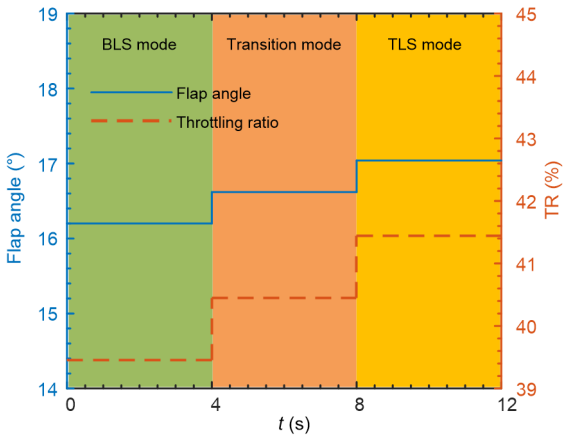

Fig. 8 Flap angle and throttling ratio

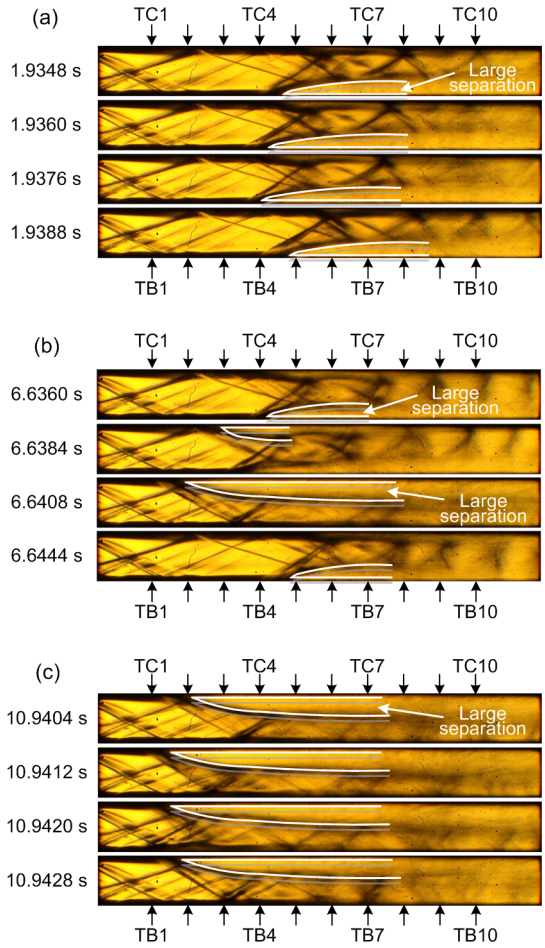

Fig. 9 Typical Schlieren images during oscillation
(a) BLS mode; (b) Transition mode; (c) TLS mode

Fig. 10a shows the typical flow structure of a shock train head in BLS mode. The simplified structure is shown in Fig. 10b. The red line indicates the isolator wall, the green line indicates the boundary layer, S1 and S2 are the leading shock waves, and S3 and S4 are two transmitted shocks formed by the intersection of S1 and S2. Considering the distribution of shock waves, the flow field can be divided into six parts. Regions u0 and d0 are located before S1 and S2. The flow parameters in these two regions are discontinuous due to the influence of the background waves. The flow in region u2, passing through shocks S2 and S4, and the flow in region d2, passing through shocks S1 and S3, should satisfy two conditions as follows.

Condition 1: The pressures must match, i.e.

$$p_{u2} = p_{d2}. \tag{3}$$

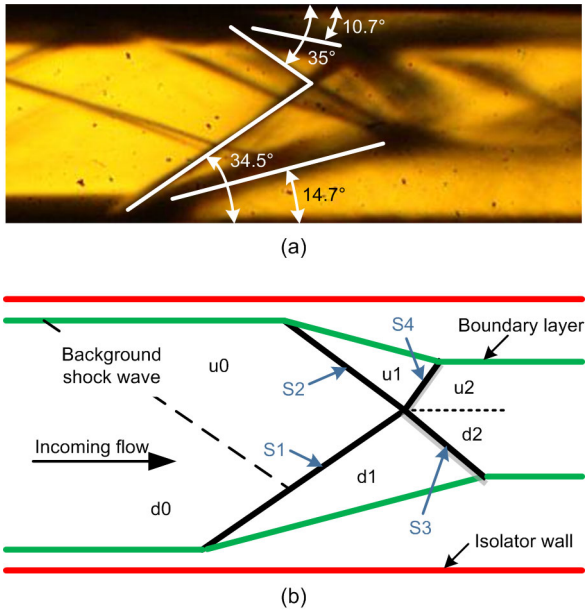

Fig. 10 Structure of shock train head
(a) Schlieren image of shock train head; (b) Simplified structure. References to color refer to the online version of this figure

Condition 2: The flow direction must be the same. In addition, due to the constraint of the isolator walls, the flow direction should be approximately parallel to the wall, i.e.

$$\varphi_{u2} = \varphi_{d2} \approx 0, \tag{4}$$

where φ is the flow angle, defined as the angle of the flow direction with respect to the horizontal direction. Positive angles mean that the flow deflects upward.

Due to the different flow parameters in regions u0 and d0 before the shock train, the size of the separation regions caused by the leading shock waves S1 and S2 is different. Next, the location of the large separation region was analyzed qualitatively. Since regions d0 and u0 are located upstream and downstream of a background shock wave respectively, the static pressure was lower in region u0 than that in region d0, i.e.

$$p_{u0} < p_{d0}. \tag{5}$$

Although the Mach numbers in regions u0 and d0 are also different, their influence on the pressure rise caused by the shock waves is not significant. For example, with the same deflection angle 10°, the

pressure ratio caused by the shock wave is 1.8 when the incoming flow Mach number is 2.30, and 1.9 when the incoming flow Mach number is 2.65. The difference in the pressure ratio due to different Mach numbers is only 0.1. As a first assumption, the difference in Mach number in regions u0 and d0 was ignored. As the flow direction is horizontal in regions u0 and u2, the deflection angles when the flow passes through shock waves S2 and S4 are the same, denoted as δ_u. Similarly, the deflection angles when the flow passes through shock waves S1 and S3 are the same, denoted as δ_d. As the pressure in regions u2 and d2 is the same, the following equation can be obtained using Eq. (5):

$$\frac{p_{u2}}{p_{u0}} > \frac{p_{d2}}{p_{d0}}. \tag{6}$$

That is to say, the pressure ratio between regions u2 and u0 is larger than that between regions d2 and d0. It is known that the flow is deflected twice by the same angle δ_u from region u0 to u2, while the flow is deflected twice by the same angle δ_d from region d0 to d2. For a flow with the same Mach number, the larger the flow deflection angle, the greater the pressure ratio caused by the shock wave. Therefore, $\delta_u > \delta_d$.

Overall, on the wall where the pressure ahead of the shock train is lower, the flow is deflected by two larger angles to generate a larger pressure ratio, so that the pressure in regions u2 and d2 after two shock waves is equal. A larger deflection angle indicates a larger separation region, so the large separation region will be formed on the wall with lower pressure.

Next, some examples of shock train heads were analyzed to validate the above conclusion. The process used for the analysis was as follows:

1. The flow parameters in regions u0 and d0 upstream of the shock train are known.

2. Assuming that the large separation region lies on the top wall or the bottom wall, the flow parameters in regions u2 and d2 can be obtained by the method of shock polar.

3. Judge whether the flow parameters in regions u2 and d2 can satisfy Eqs. (3) and (4). If so, the assumption about the location of the large separation region is correct.

Take the head of the shock train in BLS mode shown in Fig. 10a as an example. Since the pressure and Mach number of the flow in regions u0 and d0 cannot be accurately obtained from the experimental results, numerical simulations were carried out. According to the numerical results, the flow parameters in regions u0 and d0 are as follows:

$$\begin{aligned} &Ma_{u0} = 2.30,\ Ma_{d0} = 2.65,\\ &\frac{p_{u0}}{p_\infty} = 1.60,\ \frac{p_{d0}}{p_\infty} = 0.95. \end{aligned} \tag{7}$$

The flow angles in regions u1 and d1 were measured directly from the Schlieren image.

Assuming that the large separation region lies on the bottom wall, the flow angles in regions u1 and d1 are given by $\varphi_{u1}=-10.7°$ and $\varphi_{d1}=14.7°$. In Fig. 11b, the shock polar is used to solve the flow parameters in regions u2 and d2. The abscissa is the flow angle, and the ordinate is the flow static pressure normalized by the static pressure at the inlet of the isolator. The starting position of each shock polar was determined according to the flow static pressure and flow angle ahead of the shock wave, and the shock polar was plotted according to the following equations:

$$\begin{aligned} &\frac{p_2}{p_1} = \frac{2\gamma}{\gamma+1} Ma_u^2 \sin^2\beta - \frac{\gamma-1}{\gamma+1},\\ &\tan\delta = \frac{2\cot\beta\left(Ma_u^2\sin^2\beta - 1\right)}{\left[\gamma + \cos(2\beta)\right]Ma_u^2 + 2}, \end{aligned} \tag{8}$$

where p_1 and p_2 are the flow static pressures before and after the shock wave, respectively, γ is the specific heat ratio, Ma_u is the flow Mach number before the shock wave, δ is the deflection angle, and β is the shock angle.

The blue line is the shock polar for the flow in region d0, and the yellow line is the shock polar for the flow in region u0. The starting positions of the two shock polars in regions d0 and u0 are different due to the different pressures in the two regions. The red line is the shock polar for the flow in region d1, and the purple line is the shock polar for the flow in region u1. The intersections of the red and purple lines are the solutions of pressure and flow angle in regions d2 and u2. The coordinates of the intersection point are (0.1, 5.2). Therefore, $p_{u2}=p_{d2}=5.2p_\infty$, and $\varphi_{u2}=\varphi_{d2}=0.1°$. Both Eqs. (3) and (4) are satisfied.

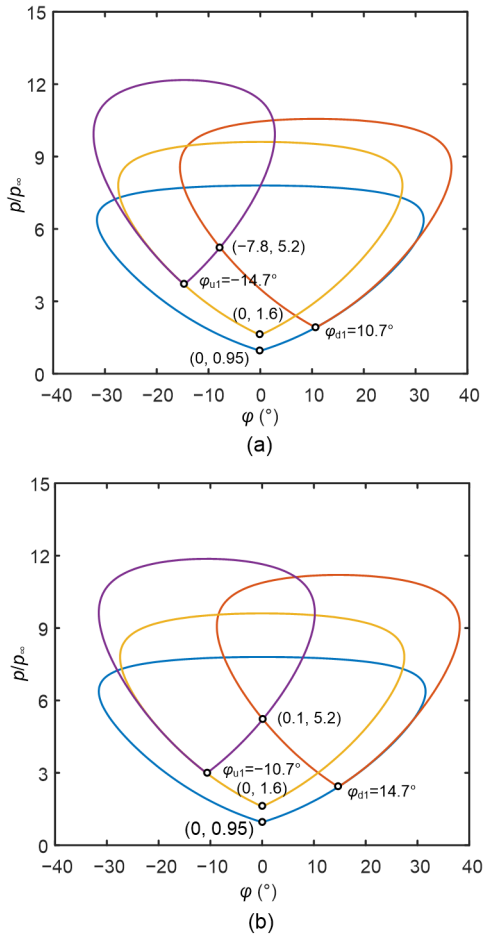

Fig. 11 Shock polars for different locations of the large separation region

(a) Large separation region on the top wall; (b) Large separation region on the bottom wall. References to color refer to the online version of this figure

Assuming that the large separation region lies on the top wall, the flow angles in regions u1 and d1 are: $\varphi_{u1}=-14.7°$, $\varphi_{d1}=10.7°$. The shock polar was used again to determine the flow parameters in regions u2 and d2 (Fig. 11a). The solutions are as follows: $p_{u2}=p_{d2}=5.2p_\infty$, $\varphi_{u2}=\varphi_{d2}=-7.8°$. It is obvious that Eq. (4) is not satisfied. Therefore, the assumption that the large separation region lies on the top wall is incorrect.

Based on the above analysis, under the incoming flow condition given in Eq. (7), the large separation region is located on the bottom wall where the wall pressure ahead of the shock train is lower. The result is consistent with the Schlieren image shown in Fig. 10a.

Take the shock train in TLS mode as an example. Fig. 12 shows the structure of the shock train head. The flow parameters ahead of the shock train obtained from numerical simulation are:

$$Ma_{u0}=2.55,\ Ma_{d0}=2.25,\quad \frac{p_{u0}}{p_\infty}=1.05,\ \frac{p_{d0}}{p_\infty}=1.65. \tag{9}$$

The shock polar was used to solve the flow parameters, as presented in Fig. 13. Assuming that the large

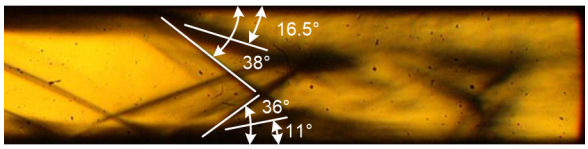

Fig. 12 Schlieren image of the shock train head in TLS mode

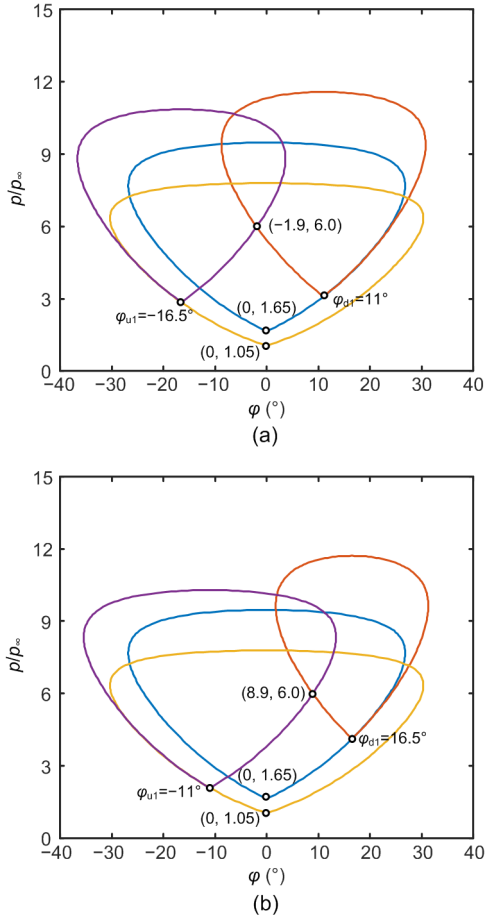

Fig. 13 Shock polars for different locations of large separation region

(a) Large separation region on the top wall; (b) Large separation region on the bottom wall. References to color refer to the online version of this figure

separation region lies on the top wall, the solutions in regions u2 and d2 are as follows: $p_{u2}=p_{d2}=6.0p_{\infty}$, $\varphi_{u2}=\varphi_{d2}=-1.9°$. Assuming the large separation region lies on the bottom wall, the solutions in regions u2 and d2 are as follows: $p_{u2}=p_{d2}=6.0p_{\infty}$, $\varphi_{u2}=\varphi_{d2}=8.9°$. The solutions under the first assumption can satisfy both Eqs. (3) and (4). Thus, the large separation region lies on the top wall where the pressure is lower.

The above analysis explains the cause of the asymmetrical structure of the shock train under the influence of background waves. The asymmetrical structure of the shock train is caused by the different pressures at the positions of STLEs on the top wall and bottom wall. To further explain the different structural changes of the shock train in different oscillation modes, we should compare the pressure at the positions of STLEs throughout the oscillation process. Compared with the unthrottled condition, pressure only in the shock train region is varied in throttled conditions. The pressure at the positions of STLEs is the same as the pressure at the same positions in the unthrottled condition. The pressure difference between two STLEs at each moment during oscillation can be obtained by the process shown in Fig. 14. First, the positions of STLEs on the top and bottom walls can be obtained from the Schlieren image of the shock train at that moment. Second, the pressure at the positions of STLEs can be determined from the wall pressure distributions. Since the wall pressure can be measured experimentally only at several discrete locations, the wall pressure distributions obtained by numerical simulation were used. Finally, the pressure difference between two STLEs can be calculated. Fig. 15 presents the position histories of STLEs obtained from Schlieren images in the experiment. The mean position of the STLE in each stage is plotted in the figure. Obviously, the oscillation of the STLE's position is much larger than the measurement error, which is equal to 0.3 mm (Section 2.1). Fig. 16 shows the change of pressure difference between two STLEs. In BLS mode, the pressure at the position of the STLE on the top wall is higher than

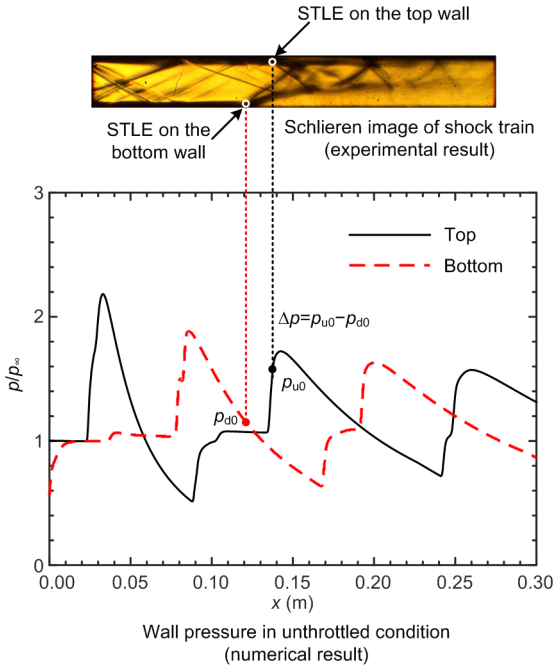

Fig. 14 Process of calculating the pressure difference Δp between two STLEs

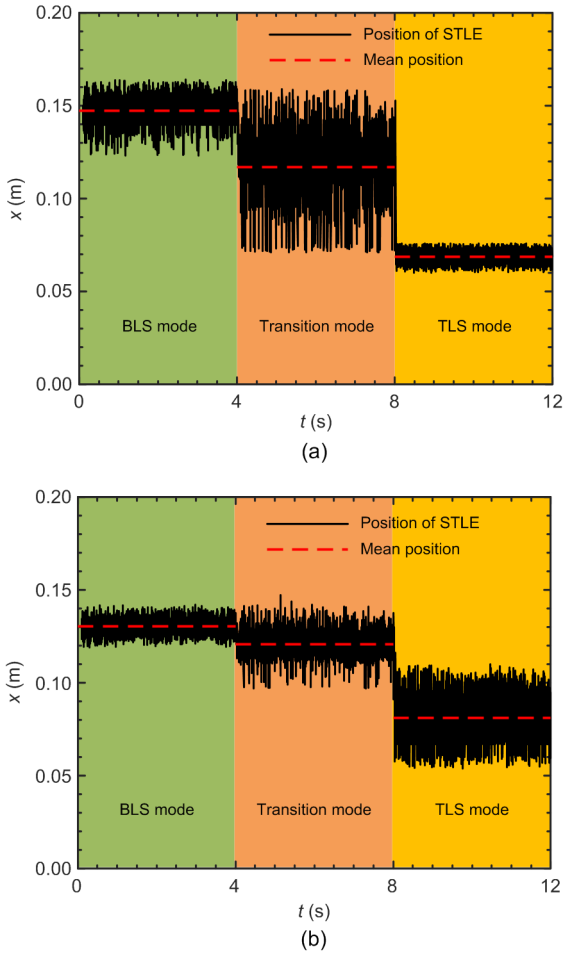

Fig. 15 Position histories of STLEs on the top wall and bottom wall

(a) Top wall; (b) Bottom wall

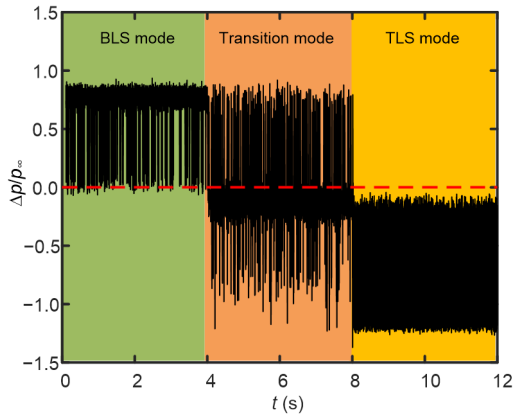

Fig. 16 History of the pressure difference between two STLEs

that on the bottom wall. Therefore, the large separation region remains on the bottom wall during oscillation. In TLS mode, the pressure at the position of the STLE on the top wall is always lower than that on the bottom wall. Thus, the large separation region remains on the top wall during oscillation. In transition mode, sometimes the pressure at the position of the STLE on the top wall is lower, and sometimes the pressure at the position of the STLE on the bottom wall is lower. Therefore, the position of the large separation region switches between the top wall and bottom wall.

In summary, the background waves in the isolator result in pressure discontinuity. The different pressures at the positions of the STLEs on the top and bottom walls cause the asymmetrical structure of the shock train. A large separation region emerges on the wall where the pressure at the position of the STLE is lower, and the shock train deflects toward the other wall. In the shock train self-excited oscillation, the mode of the shock train is related to the change of pressure at the positions of the STLEs on both walls during the whole oscillation process.

3.3 Effect of the wall pressure gradient on shock train self-excited oscillation

Many studies have shown that the wall pressure gradient at the position of the STLE would affect the shock train behavior when it moves upstream (Tan et al., 2012; Xu et al., 2016; Li et al., 2018). We suspect that the wall pressure gradient would also affect shock train self-excited oscillation. To determine the effect of the wall pressure gradient, we compared the oscillation characteristics of STLEs and the wall pressure gradient in the oscillation range of STLEs. Fig. 17 presents the oscillation ranges of STLEs in

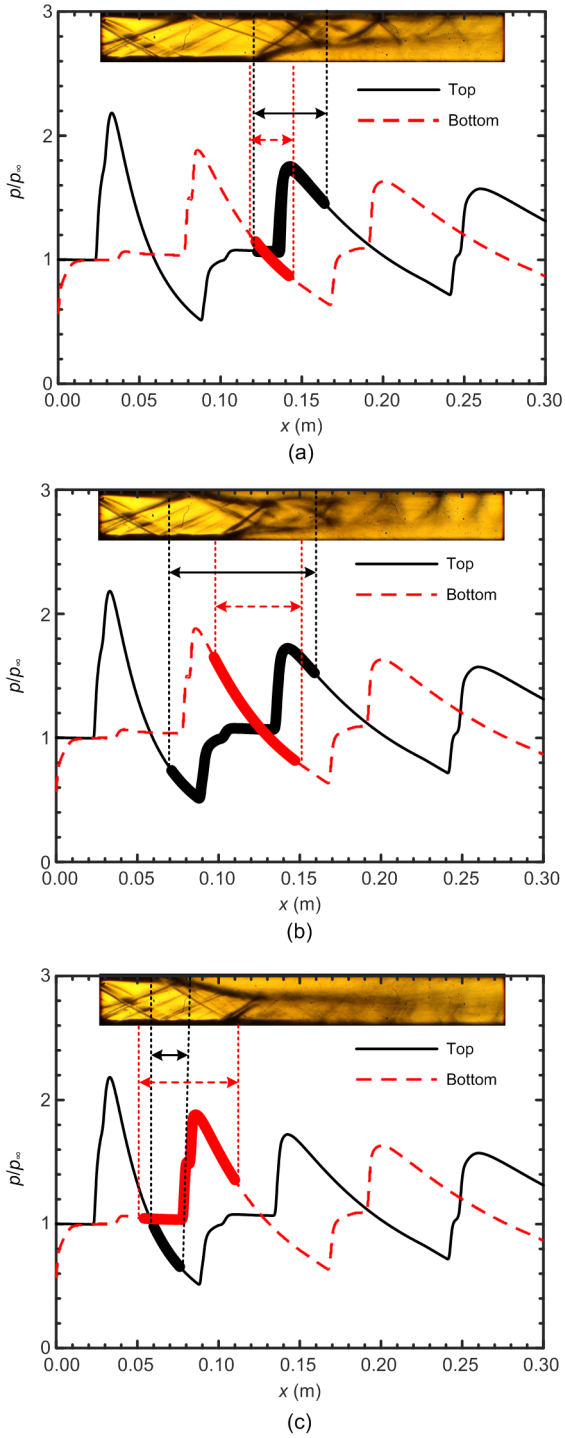

Fig. 17 Wall pressure distributions (numerical results) and oscillation ranges of STLEs (experimental results)
(a) BLS mode; (b) Transition mode; (c) TLS mode

different oscillation modes, obtained from Fig. 15. The solid arrow indicates the oscillation range of STLE on the top wall, and the dashed arrow indicates the oscillation range of STLE on the bottom wall. As we are concerned only with the wall pressure upstream of the shock train and the pressure in this region remains the same as the pressure in the unthrottled condition, the wall pressure distributions in the unthrottled condition obtained by numerical simulation are shown in Fig. 17. Then the wall pressure gradient in the oscillation ranges of STLEs can be determined. The results are presented in Table 2.

Table 2 Wall pressure gradient with respect to x at the position of the STLE in different oscillation modes

Oscillation mode	Wall pressure gradient with respect to x	
	Top wall	Bottom wall
BLS mode	Negative	Positive
Transition mode	Negative	Positive
TLS mode	Positive	Negative

To compare the oscillation intensity of STLEs on the top and bottom walls, the moving standard deviation of the STLE was calculated with a time window of 200 ms. The results are shown in Fig. 18, which also contains a plot of the throttling ratio history. At 4 s and 8 s, the oscillation mode of the shock train changes due to the variation of the throttling ratio at the isolator exit. Thus, the standard deviations of the STLEs on both the top and bottom walls change sharply at these two moments. When the shock train is in BLS or transition mode, the standard deviation of the STLE on the top wall is always greater than that on the bottom wall, indicating that the STLE on the top wall oscillates more severely. Table 2 shows that, in BLS or transition mode, the STLE on the top wall lies in a negative pressure gradient region, while the STLE on the bottom wall lies in a positive pressure gradient region. When the shock train is in TLS mode, the standard deviation of the STLE on the bottom wall is larger than that on the top wall, indicating that the STLE on the bottom wall oscillates more severely. In this mode, the STLE on the bottom wall lies in a negative pressure gradient region, while the STLE on the top wall lies in a positive pressure gradient region. By comparing the standard deviation of the STLE on the top wall with that of the STLE on the bottom wall, it can be seen that the STLE lying in a negative pressure gradient region oscillates more violently than the STLE lying in a positive pressure gradient region, no matter which oscillation mode the shock train is in.

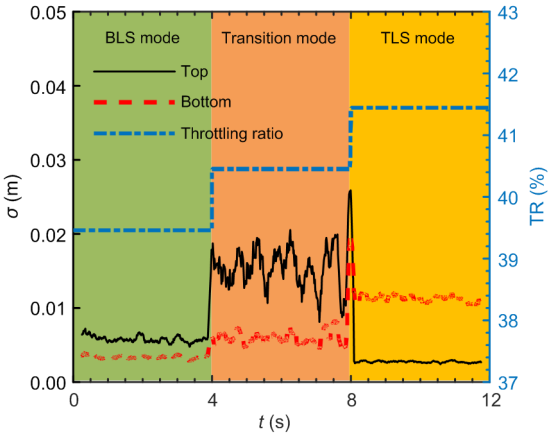

Fig. 18 Moving standard deviations σ of positions of STLEs on the top and bottom walls

Comparing the standard deviations of the STLE on the top wall in different oscillation modes shows that the standard deviation in TLS mode is the smallest. At this time, the STLE on the top wall is in a positive pressure gradient region. When the shock train is in BLS mode or transition mode, the STLE on the top wall lies in a negative pressure gradient region. However, in transition mode, the oscillation range of the STLE on the top wall contains two negative pressure gradient regions (Fig. 17b). Thus, the standard deviation in transition mode is the largest. Comparing the standard deviations of the STLE on the bottom wall shows that the standard deviation is the largest when the STLE on the bottom wall lies in a negative pressure gradient region. To summarize, whether on the top or the bottom wall, when the STLE is in the negative pressure gradient region, its oscillation will be strengthened, but when the STLE is in the positive pressure gradient region, its oscillation will be weakened.

The moving standard deviation can reflect the average oscillation intensity of the STLE in the time window. The maximum oscillation amplitude of the STLE is also important for the shock train, since

excessive oscillation amplitude may cause inlet unstart. Fig. 19 presents the oscillation amplitudes of STLEs on the top and bottom walls in different modes. In BLS mode or transition mode, the oscillation amplitude of the STLE on the top wall is larger than that on the bottom wall. In TLS mode, the oscillation amplitude of the STLE on the bottom wall is larger than that on the top wall. Combined with Table 2, it can be found that the oscillation amplitude of the STLE is larger on the wall where the pressure gradient is negative, regardless of the oscillation mode of the shock train. Comparing the oscillation amplitudes of the STLE on the top wall in different modes shows that the oscillation amplitude reaches a maximum when the STLE lies in a negative pressure gradient region. Comparing the oscillation amplitudes of the STLE on the bottom wall in different modes, the same conclusion can be reached. Therefore, when the STLE lies in the negative pressure gradient region, the oscillation amplitude is bigger; when it lies in the positive pressure gradient region, the oscillation amplitude is smaller.

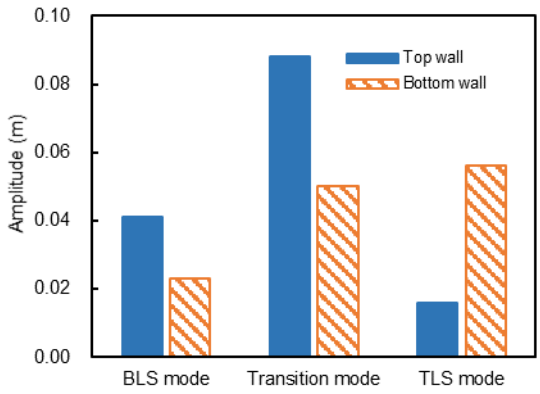

Fig. 19 Oscillation amplitudes of STLEs in different modes

To further analyze the influence of the wall pressure gradient on the frequency f of shock train self-excited oscillation, the fast Fourier transform was used to obtain the amplitude spectra of the STLEs on the top and bottom walls. The results in different modes are shown in Fig. 20. No matter which oscillation mode the shock train is in, the oscillation of the STLE has no obvious dominant frequency. The oscillation frequency is mainly below 1000 Hz. When the shock train is in BLS mode or transition mode, the STLE on the top wall lies in a negative pressure gradient region, and the STLE on the bottom wall lies in a positive pressure gradient region. The STLE on the top wall oscillates more over the whole frequency range than the STLE on the bottom wall (Fig. 20). When the shock train is in TLS mode, the STLE on

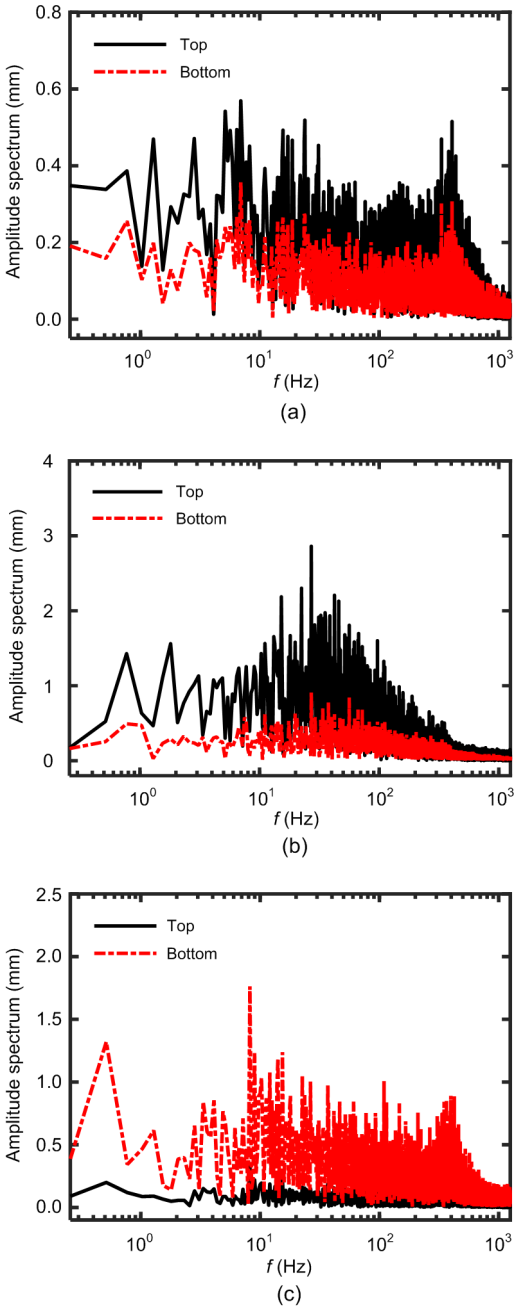

Fig. 20 Amplitude spectra of STLEs in different modes
(a) BLS mode; (b) Transition mode; (c) TLS mode

the bottom wall lies in a negative pressure gradient region, and the STLE on the top wall lies in a positive pressure gradient region. The oscillation of the STLE on the bottom wall is stronger than that on the top wall over the entire frequency range. Therefore, when the STLE lies in a negative pressure gradient region, its oscillation will be increased over the entire frequency range, regardless of the oscillation mode of the shock train.

3.4 Source of perturbation of shock train self-excited oscillation

Shock train motion is caused by internal or external perturbations. During the perturbation propagation process, a pressure fluctuation is induced as the perturbation travels past the transducer. The synchronicity of the pressure change at different locations can be obtained by coherence analysis, and whether these pressure changes are caused by the same perturbation source can be judged. Therefore, coherence analysis was performed on the wall pressure when the shock train is in different oscillation modes. The coherence $C_{xy}(f)$ between signals $x(t)$ and $y(t)$ is defined as

$$C_{xy}(f)=\frac{\left|P_{xy}(f)\right|^2}{P_{xx}(f)P_{yy}(f)}, \tag{10}$$

where $P_{xx}(f)$ and $P_{yy}(f)$ are the power spectral densities of signals $x(t)$ and $y(t)$, respectively, and $P_{xy}(f)$ is the cross power spectral density of signals $x(t)$ and $y(t)$. $P_{xy}(f)$ can be expressed as

$$P_{xy}(f)=G_{xy}(f)-\mathrm{i}Q_{xy}(f)=\left|P_{xy}(f)\right|\mathrm{e}^{-\mathrm{i}Q_{xy}(f)}, \tag{11}$$

where $G_{xy}(f)$ and $Q_{xy}(f)$ denote the real and imaginary parts of $P_{xy}(f)$. The phase lag between signals $x(t)$ and $y(t)$ is defined as

$$\mathrm{Lag}(f)=\arctan\frac{Q_{xy}(f)}{G_{xy}(f)}. \tag{12}$$

In shock train self-excited oscillation, since the pressure in the oscillation range of the STLE changes first due to the back and forth movements of the STLE, the pressure signal p_i in the oscillation range of the STLE is selected to calculate its coherences with pressure signal p_j at other locations. Fig. 21 shows the calculated coherence distributions. The abscissa represents the streamwise locations of pressure signals, and the ordinate represents the frequency range of pressure signals. Because the coherence of pressure signals with frequencies above 1000 Hz is small, it is not shown in the figure. The coherence of the pressure signal at locations between pressure transducers is obtained by linear interpolation of the coherence of pressure signals at positions of two adjacent pressure transducers. Since the coherence between p_i and itself equals 1, it is not shown in Fig. 21, to avoid its high value affecting the resolution of other coherence distributions. The positions of transducers are marked with arrows.

Fig. 21 presents the contours of wall pressure coherence when the shock train is in BLS mode. Since TC5 lies in the oscillation range of the STLE on the top wall, the coherence on the top wall is calculated with the pressure at TC5 and other locations. Along the top wall, the coherence between the pressure at TC5 and the pressure at TC6–TC8 is high, and the frequency with high coherence is concentrated mainly below 50 Hz and around 400 Hz. As seen from the Schlieren image in Fig. 9, TC6–TC8 are located between the leading shock and the second shock inside the shock train. The pressure perturbations can travel in the small separation region and this zone is unaffected by other strong perturbations. Therefore, the coherence in this zone is high. The second shock lies near TC8. The pressure downstream of the second shock is affected mainly by the motion of this shock, so the coherence between it and pressure at TC5 is weak. The coherence on the bottom wall is calculated using the pressure at TB4 and other locations. Along the bottom wall, the pressures downstream of TB4 all show a high coherence, because a large separation region is formed from the STLE and extends to the exit of the isolator. In this large separation region, the pressure perturbations can propagate freely and the effect of internal shock waves on the wall pressure is isolated. Similarly, the frequency with high coherence is also concentrated below 50 Hz and around 400 Hz on the bottom wall.

Fig. 22 presents the contours of wall pressure coherence when the shock train is in TLS mode. TC1

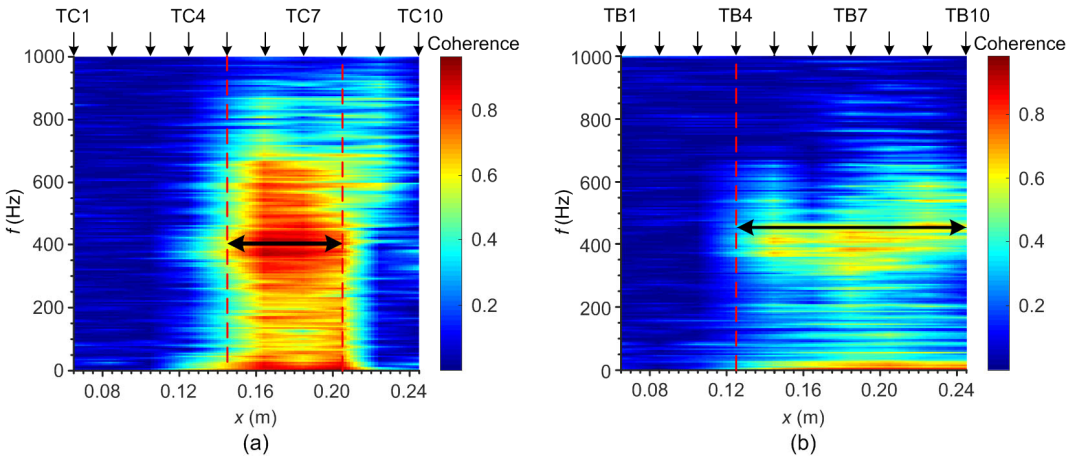

Fig. 21 Contours of wall pressure coherence in BLS mode
(a) Top wall; (b) Bottom wall

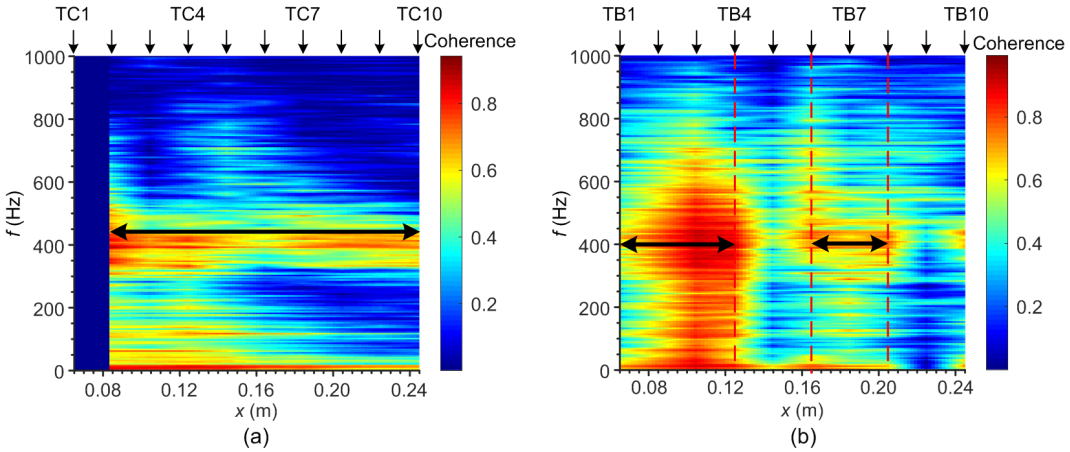

Fig. 22 Contours of wall pressure coherence in TLS mode
(a) Top wall; (b) Bottom wall

on the top wall and TB2 on the bottom wall are located in the oscillation range of the STLE, and thus coherence is calculated using the pressure at these two locations and other locations. In TLS mode, the large separation region is on the top wall, and the pressure downstream of TC1 shows high coherence. On the bottom wall, the coherence between the pressures at TB2 and downstream locations is discontinuous at the locations of TB5 and TB9. The discontinuity is caused by shocks inside the shock train. The high coherence region where TB3 and TB4 are located is directly connected to TB2. The high coherence in this region is caused by the propagation of the perturbations in the small separation region induced by the leading shock. The high coherence region where TB6–TB8 lie and the high coherence region where TB10 lies are caused by the motion of the entire shock train.

Comparison of the coherence distributions of the wall pressure when the shock train is in TLS and BLS modes shows that the coherence distribution is related to the size of separation region. On the wall with a large separation region, the pressure in the oscillation range of the STLE has high coherence with pressure at all downstream locations. On the wall with a small separation region, the high coherence region downstream of the oscillation range of the STLE is discontinuous. However, the coherence between the pressure in the oscillation range of the STLE and the pressure in the separation region induced by the leading shock retains a high value, regardless of

whether the separation region is large or small. The unsteady movement of the STLE is closely related to the unsteady pressure change in the downstream separation region. However, whether the movement of the STLE causes the downstream pressure change or the downstream pressure change causes the movement of the STLE was still unknown. Next, phase analysis was performed to find the answer.

As the behavior of the shock train in TLS or BLS mode is similar, except for the position of the large separation region, the shock train motion in BLS mode was taken as an example for analysis. Fig. 23

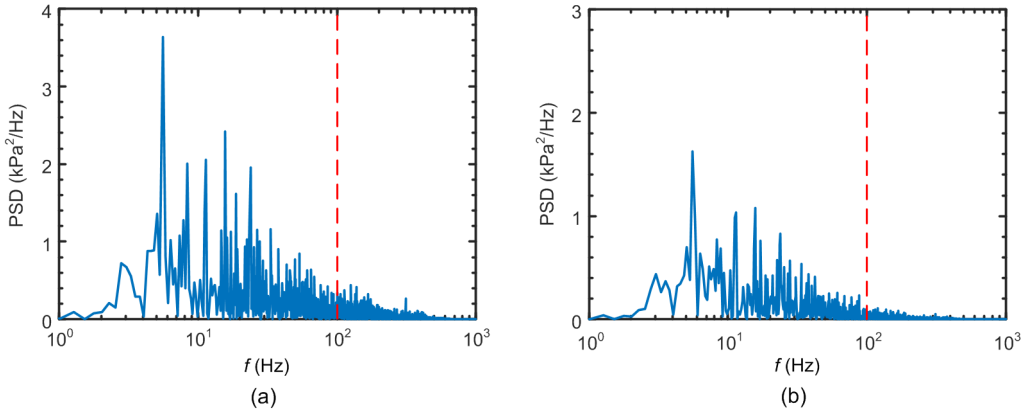

Fig. 23 PSDs of pressures at TC5 and TB4
(a) TC5; (b) TB4

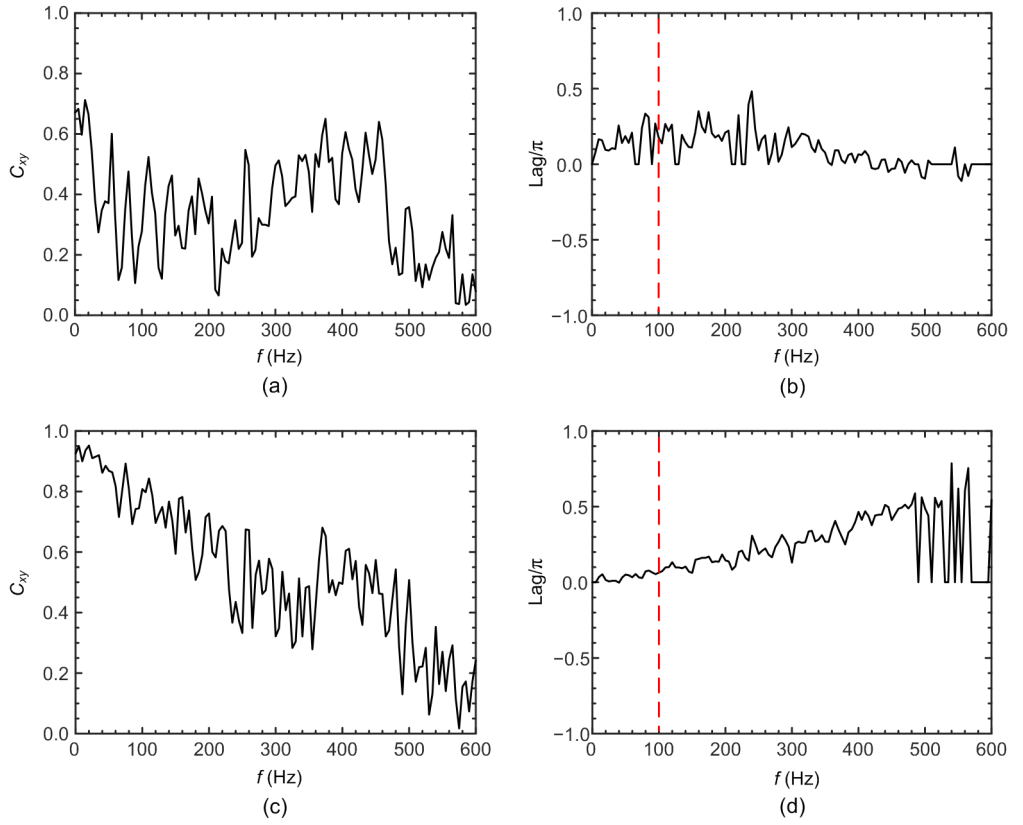

Fig. 24 Coherence and phase lags on the bottom wall in BLS mode
(a) Coherence between pressures at TB6 and TB4; (b) Phase lag between pressures at TB6 and TB4; (c) Coherence between pressures at TB6 and TB8; (d) Phase lag between pressures at TB6 and TB8

presents the power spectral densities (PSDs) of pressures at TC5 and TB4, as they are in the oscillation range of the STLE. The frequencies with high values of PSD are below 100 Hz, indicating most of the oscillation energy is concentrated in this frequency range. Thus, only the phase lag of pressure signals with a frequency below100 Hz is discussed below.

The pressure on the bottom wall is analyzed first, as there is only one large separation region and the flow structure is simple. Fig. 24 (p.629) shows the coherence and phase lags between pressures at TB6 and TB4, TB8. The phase lags between pressures at TB6 and TB4, and at TB6 and TB8, are positive when the frequency is below 100 Hz. That is to say, the pressure changes at TB4 and TB8 all occur after that at TB6. The pressure perturbation is first generated at TB6 and then propagates upstream and downstream. The perturbation propagating upstream causes oscillation of the STLE. There are several high coherence regions on the top wall, but only the region adjacent to TC5 is analyzed because the high coherence in this region is caused by the propagation of perturbation. Fig. 25 shows the coherence and phase lags between pressures at TC7 and TC5, TC8. The phase lags between TC7 and TC5, and between TC7 and TC8, are positive when the frequency is below 100 Hz. This indicates that the oscillation of the STLE on the top wall is caused by the perturbation at TC7. Both TB6 and TC7 are located in the separation region induced by the leading shock (Fig. 9).

When the shock train is in transition mode, TC2 on the top wall and TB4 on the bottom wall are located in the oscillation range of the STLE. The coherence of pressures at these two positions with pressures at other positions is shown in Fig. 26. On both walls, the high coherence region is discontinuous because the large separation region cannot be stabilized on one wall. When the location of the large separation region switches from one wall to another, the downstream propagation of perturbation is

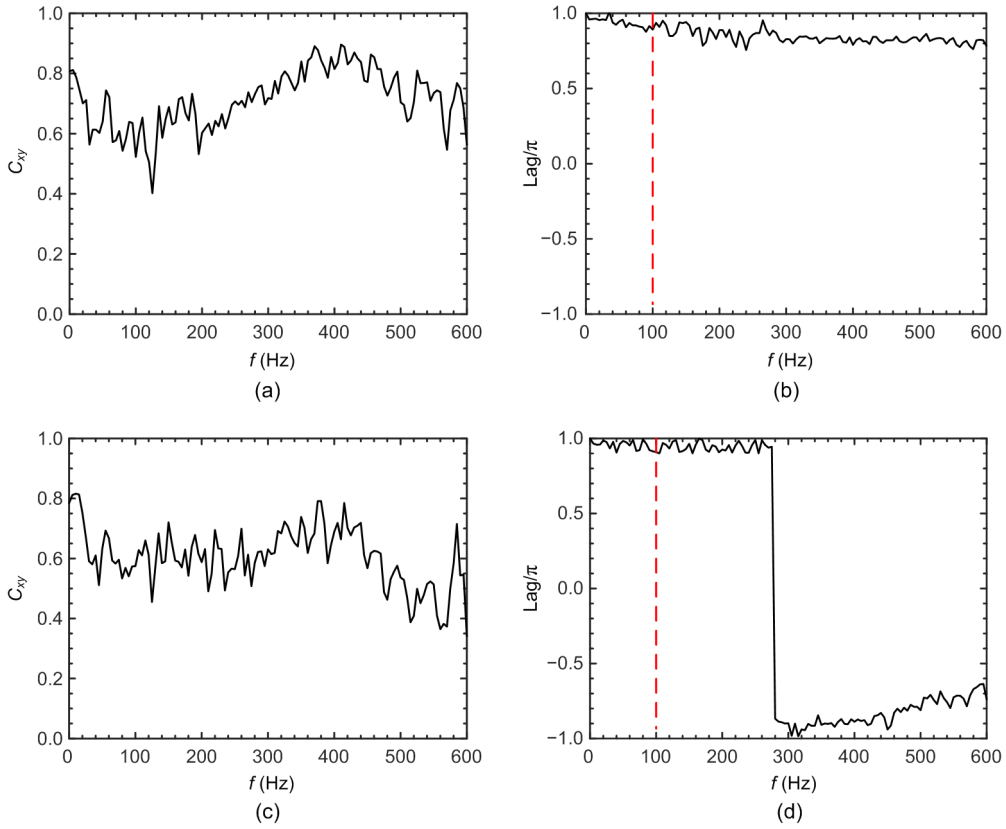

Fig. 25 Coherence and phase lags on the top wall in BLS mode

(a) Coherence between pressures at TC7 and TC5; (b) Phase lag between pressures at TC7 and TC5; (c) Coherence between pressures at TC7 and TC8; (d) Phase lag between pressures at TC7 and TC8

blocked. The phase lags were also calculated (Fig. 27). The pressure perturbation originates from TC5 on the top wall, and from TB4 on the bottom wall. Both TC5 and TB4 are located in the separation region induced by the leading shock (Fig. 9).

From the above analysis, it can be seen that shock train self-excited oscillation is caused by the pressure perturbation in the downstream separation

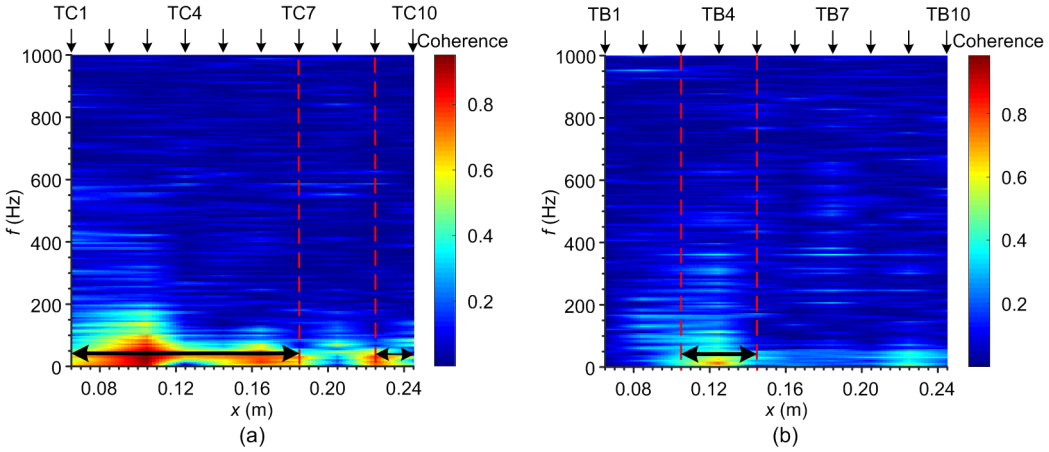

Fig. 26 Contours of wall pressure coherence in transition mode

(a) Top wall; (b) Bottom wall

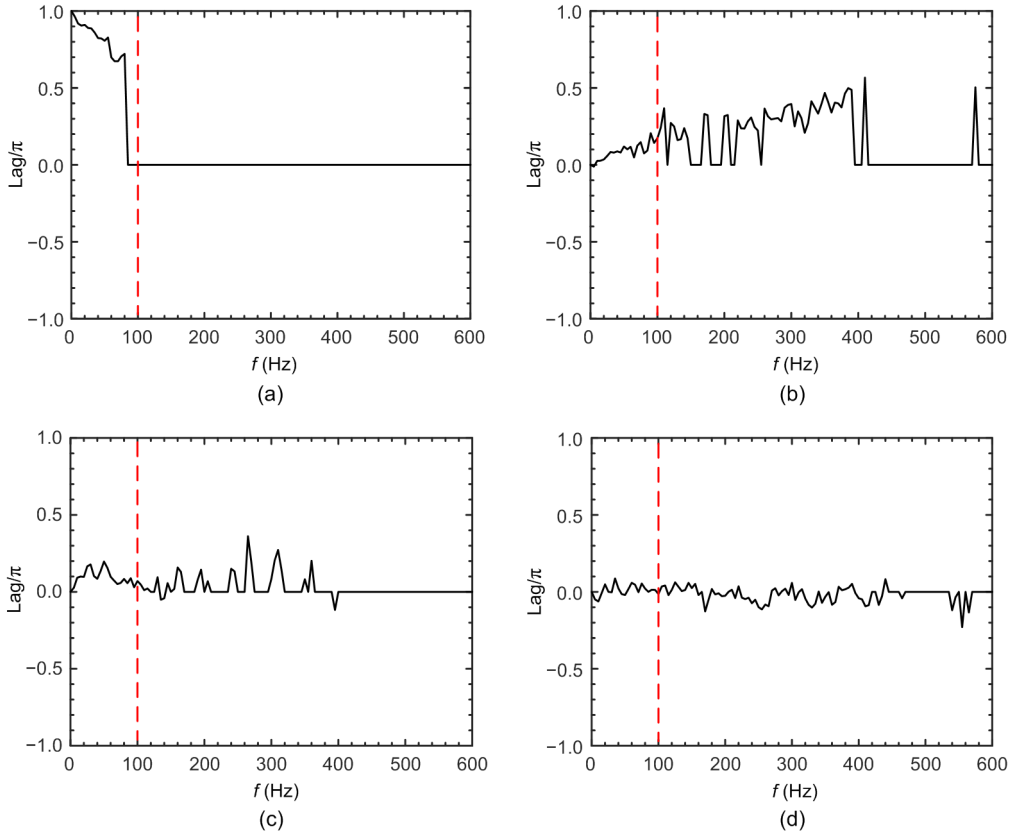

Fig. 27 Phase lags in transition mode

(a) Phase lag between pressures at TC5 and TC2; (b) Phase lag between pressures at TC5 and TC7; (c) Phase lag between pressures at TB4 and TB3; (d) Phase lag between pressures at TB4 and TB5

region induced by the leading shock, regardless of the mode of self-excited oscillation.

3.5 Schematic of shock train self-excited oscillation

According to the analysis above, the mechanism of shock train self-excited oscillation in an isolator with background waves can be obtained. The schematic diagram of the mechanism is shown in Fig. 28. Because of the existence of asymmetrical back groundwaves, the pressure distribution on the top and bottom walls of the isolator differs. The pressure at the position of the STLE on the bottom wall is lower than that on the top wall; thus, a large separation region is formed on the bottom wall and a small separation region on the top wall. A perturbation is generated in the large separation region due to the instability of separation, and propagates upstream and downstream. The perturbation propagating upstream reaches the position of the STLE on the bottom wall, causing movement of the STLE, while the perturbation propagating downstream reaches the exit of the isolator. Similarly, a perturbation is generated in the small separation region after the STLE on the top wall. The perturbation propagating upstream also causes the STLE on the top wall to move, while the perturbation propagating downstream reaches the second shock in the shock train, after which the propagation is blocked. The movement of both STLEs causes motion of the entire shock train and the change of flow structure inside the shock train. Since the core flow of the shock train deflects to the top wall and the internal shock waves directly act on the top wall, the pressure changes greatly along the top wall. The oscillation range of the STLE is related to the wall pressure gradient formed by the background waves. The STLE on the top wall lies in a negative pressure gradient region, and the STLE on the bottom wall lies in a positive pressure gradient region, so the STLE on the top wall has a larger oscillation range. In addition, if the STLE on the top wall passes over the shock reflection point for a long distance, the pressure at the position of the STLE on the top wall will be lower than that on the bottom wall, causing the position of the large separation region to be switched from the bottom wall to the top wall. Thus, the mode of the shock train self-excited oscillation is related to the pressure change in the oscillation range of the STLE on both walls, and the oscillation range is related to the wall pressure gradient.

4 Conclusions

Many researchers have studied shock train self-excited oscillation in isolators without background waves and discussed the mechanism. However, there have been few studies on self-excited oscillation in isolators with background waves. In previous study (Hou et al., 2020), we described in detail the behavior of a shock train during self-excited oscillation affected by background waves, and compared it with self-excited oscillation without background waves, but how the background waves affect the oscillation was still unclear. In this study, we investigated experimentally the shock train self-excited oscillation in an isolator with background waves. The cause of the

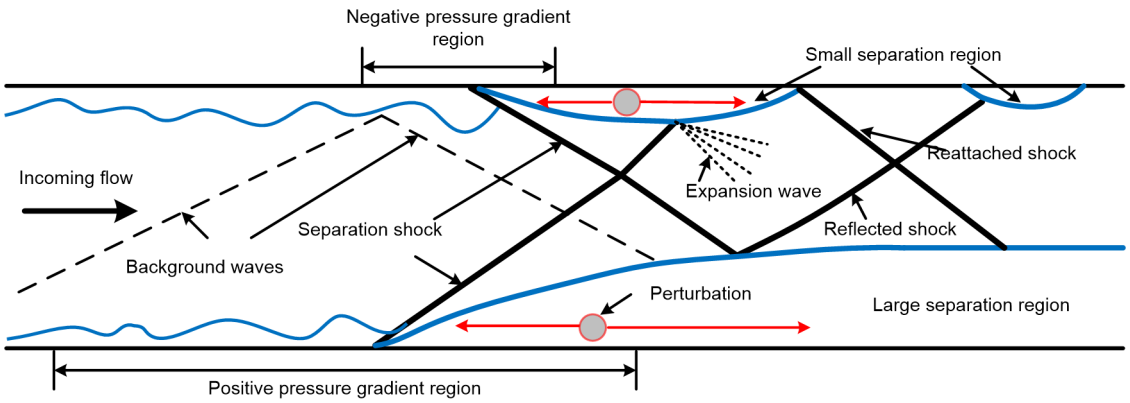

Fig. 28 Schematic diagram of the mechanism of shock train self-excited oscillation

asymmetrical structure of the shock train was analyzed and the effect of the wall pressure gradient was determined. Coherence and phase analysis were performed to reveal the source of perturbation that causes shock train self-excited oscillation. The main conclusions were as follows:

1. The pressure discontinuity induced by background waves causes the asymmetry of the shock train structure. On the wall where the pressure at the location of the STLE is lower, a large separation region is formed and the shock train deflects toward the other wall. During shock train self-excited oscillation, the oscillation mode depends on the magnitude of the change of pressure in the oscillation range of the STLEs on the top and bottom walls.

2. The wall pressure gradient induced by background waves affects the oscillation range and oscillation intensity of the STLE. When the STLE lies in a negative pressure gradient region, the oscillation amplitude of the STLE increases, and oscillation strengthens over the whole frequency range. Conversely, when the STLE lies in a positive pressure gradient region, the oscillation amplitude of the STLE decreases, and oscillation weakens over the whole frequency range. The influence of the wall pressure gradient on the STLE is independent of the oscillation mode of the shock train.

Coherence analysis of wall pressure indicated that, regardless of the oscillation mode of the shock train, on the wall where the large separation region can stably exist, there is a continuous high coherence region, which extends to the isolator exit; on the wall where the large separation region cannot stably exist, or where the small separation region exists, there are several discontinuous high coherence regions due to the influence of shock waves inside the shock train. However, no matter which type of wall, phase analysis in the frequency range with high coherence indicated that the pressure in the separation region induced by the leading shock changes first. This demonstrates that the perturbation caused by instability of the separation region triggers unstable shock train self-excited oscillation.

Contributors

Wen-xin HOU designed the research. Wen-xin HOU and Chen KONG processed the corresponding data. Wen-xin HOU wrote the first draft of the manuscript. Jun-tao CHANG, Wen BAO, and Laurent DALA helped to organize the manuscript. Wen-xin HOU revised and edited the final version.

Conflict of interest

Wen-xin HOU, Jun-tao CHANG, Chen KONG, Wen BAO, and Laurent DALA declare that they have no conflict of interest.

References

Cai JH, Zhou J, Liu SJ, et al., 2017. Effects of dynamic backpressure on shock train motions in straight isolator. *Acta Astronautica*, 141:237-247. https://doi.org/10.1016/j.actaastro.2017.10.013

Carroll BF, Dutton JC, 1990. Characteristics of multiple shock wave/turbulent boundary-layer interactions in rectangular ducts. *Journal of Propulsion and Power*, 6(2):186-193. https://doi.org/10.2514/3.23243

Fiévet R, Koo H, Raman V, et al., 2017. Numerical investigation of shock-train response to inflow boundary-layer variations. *AIAA Journal*, 55(9):2888-2901. https://doi.org/10.2514/1.J055333

Geerts JS, Yu KH, 2016. Shock train/boundary-layer interaction in rectangular isolators. *AIAA Journal*, 54(11):3450-3464. https://doi.org/10.2514/1.J054917

Gnani F, Zare-Behtash H, Kontis K, 2016. Pseudo-shock waves and their interactions in high-speed intakes. *Progress in Aerospace Sciences*, 82:36-56. https://doi.org/10.1016/j.paerosci.2016.02.001

Hou WX, Chang JT, Xie ZQ, et al., 2020. Behavior and flow mechanism of shock train self-excited oscillation influenced by background waves. *Acta Astronautica*, 166:29-40. https://doi.org/10.1016/j.actaastro.2019.09.032

Huang W, Wang ZG, Pourkashanian M, et al., 2011. Numerical investigation on the shock wave transition in a three-dimensional scramjet isolator. *Acta Astronautica*, 68(11-12):1669-1675. https://doi.org/10.1016/j.actaastro.2010.12.011

Hunt RL, Gamba M, 2018. Shock train unsteadiness characteristics, oblique-to-normal transition, and three-dimensional leading shock structure. *AIAA Journal*, 56(4):1569-1587. https://doi.org/10.2514/1.J056344

Ikui T, Matsuo K, Nagai M, et al., 1974. Oscillation phenomena of pseudo-shock waves. *Bulletin of JSME*, 17(112):1278-1285. https://doi.org/10.1299/jsme1958.17.1278

Jiao XL, Chang JT, Wang ZQ, et al., 2016. Investigation of hypersonic inlet pulse-starting characteristics at high Mach number. *Aerospace Science and Technology*, 58:427-436. https://doi.org/10.1016/j.ast.2016.09.008

Li N, Chang JT, Xu KJ, et al., 2017. Prediction dynamic model

of shock train with complex background waves. *Physics of Fluids*, 29(11):116103. https://doi.org/10.1063/1.5000876

Li N, Chang JT, Xu KJ, et al., 2018. Oscillation of the shock train in an isolator with incident shocks. *Physics of Fluids*, 30(11):116102. https://doi.org/10.1063/1.5053451

Liao L, Yan L, Huang W, et al., 2018. Mode transition process in a typical strut-based scramjet combustor based on a parametric study. *Journal of Zhejiang University-SCIENCE A (Applied Physics & Engineering)*, 19(6): 431-451. https://doi.org/10.1631/jzus.A1700617

Lu L, Wang Y, Fan XQ, et al., 2018. Numerical investigation of shock train unsteady movement in a mixing duct. *Aerospace Science and Technology*, 81:375-382. https://doi.org/10.1016/j.ast.2018.08.027

Matsuo K, Miyazato Y, Kim HD, 1999. Shock train and pseudo-shock phenomena in internal gas flows. *Progress in Aerospace Sciences*, 35(1):33-100. https://doi.org/10.1016/S0376-0421(98)00011-6

Raj NOP, Venkatasubbaiah K, 2012. A new approach for the design of hypersonic scramjet inlets. *Physics of Fluids*, 24(8):086103. https://doi.org/10.1063/1.4748130

Shi W, Chang JT, Ma JC, et al., 2019a. Path dependence characteristic of shock train in a 2D hypersonic inlet with variable background waves. *Aerospace Science and Technology*, 86:650-658. https://doi.org/10.1016/j.ast.2019.02.001

Shi W, Chang JT, Zhang JL, et al., 2019b. Numerical investigation on the forced oscillation of shock train in hypersonic inlet with translating cowl. *Aerospace Science and Technology*, 87:311-322. https://doi.org/10.1016/j.ast.2019.02.022

Smirnov NN, Betelin VB, Shagaliev RM, et al., 2014. Hydrogen fuel rocket engines simulation using LOGOS code. *International Journal of Hydrogen Energy*, 39(20): 10748-10756. https://doi.org/10.1016/j.ijhydene.2014.04.150

Smirnov NN, Betelin VB, Nikitin VF, et al., 2015. Accumulation of errors in numerical simulations of chemically reacting gas dynamics. *Acta Astronautica*, 117:338-355. https://doi.org/10.1016/j.actaastro.2015.08.013

Su WY, Zhang KY, 2013. Back-pressure effects on the hypersonic inlet-isolator pseudoshock motions. *Journal of Propulsion and Power*, 29(6):1391-1399. https://doi.org/10.2514/1.B34803

Su WY, Chen Y, Zhang FR, et al., 2018. Control of pseudo-shock oscillation in scramjet inlet-isolator using periodical excitation. *Acta Astronautica*, 143:147-154. https://doi.org/10.1016/j.actaastro.2017.10.040

Sugiyama H, Takeda H, Zhang JP, et al., 1988. Locations and oscillation phenomena of pseudo-shock waves in a straight rectangular duct. *JSME International Journal Ser. 2, Fluids Engineering, Heat Transfer, Power, Combustion, Thermophysical Properties*, 31(1):9-15. https://doi.org/10.1299/jsmeb1988.31.1_9

Sugiyama H, Tsujiguchi Y, Honma T, 2008. Structure and oscillation phenomena of pseudo-shock waves in a straight square duct at Mach 2 and 4. Proceedings of the 15th AIAA International Space Planes and Hypersonic Systems and Technologies Conference, p.2646. https://doi.org/10.2514/6.2008-2646

Tam CJ, Hsu KY, Hagenmaier M, et al., 2013. Studies of inlet distortion in a direct-connect axisymmetric scramjet isolator. *Journal of Propulsion and Power*, 29(6):1382-1390. https://doi.org/10.2514/1.b34944

Tan HJ, Sun S, Huang HX, 2012. Behavior of shock trains in a hypersonic inlet/isolator model with complex background waves. *Experiments in Fluids*, 53(6):1647-1661. https://doi.org/10.1007/s00348-012-1386-1

Wagner JL, Yuceil KB, Valdivia A, et al., 2009. Experimental investigation of unstart in an inlet/isolator model in Mach 5 flow. *AIAA Journal*, 47(6):1528-1542. https://doi.org/10.2514/1.40966

Waltrup PJ, Billig FS, 1973. Structure of shock waves in cylindrical ducts. *AIAA Journal*, 11(10):1404-1408. https://doi.org/10.2514/3.50600

Wang CP, Cheng C, Cheng KM, et al., 2018. Unsteady behavior of oblique shock train and boundary layer interactions. *Aerospace Science and Technology*, 79:212-222. https://doi.org/10.1016/j.ast.2018.05.054

Wen X, Liu J, Li J, et al., 2019. Design and numerical simulation of a clamshell-shaped inlet cover for air-breathing hypersonic vehicles. *Journal of Zhejiang University-SCIENCE A (Applied Physics & Engineering)*, 20(5): 347-357. https://doi.org/10.1631/jzus.A1800620

Xing F, Ruan C, Huang Y, et al., 2017. Numerical investigation on shock train control and applications in a scramjet engine. *Aerospace Science and Technology*, 60:162-171. https://doi.org/10.1016/j.ast.2016.11.007

Xiong B, Wang ZG, Fan XQ, et al., 2017a. Experimental study on the flow separation and self-excited oscillation phenomenon in a rectangular duct. *Acta Astronautica*, 133: 158-165. https://doi.org/10.1016/j.actaastro.2017.01.009

Xiong B, Fan XQ, Wang Y, et al., 2017b. Back-pressure effects on unsteadiness of separation shock in a rectangular duct at Mach 3. *Acta Astronautica*, 141:248-254. https://doi.org/10.1016/j.actaastro.2017.09.032

Xu KJ, Chang JT, Zhou WX, et al., 2016. Mechanism and prediction for occurrence of shock-train sharp forward movement. *AIAA Journal*, 54(4):1403-1412. https://doi.org/10.2514/1.J054577

Xu KJ, Chang JT, Zhou WX, et al., 2017. Mechanism of shock

train rapid motion induced by variation of attack angle. *Acta Astronautica*, 140:18-26. https://doi.org/10.1016/j.actaastro.2017.08.009

Xu KJ, Chang JT, Li N, et al., 2018. Experimental investigation of mechanism and limits for shock train rapid forward movement. *Experimental Thermal and Fluid Science*, 98:336-345. https://doi.org/10.1016/j.expthermflusci.2018.06.015

Yamane R, Kondo E, Tomita Y, et al., 1984. Vibration of pseudo-shock in straight duct: 1st report, fluctuation of static pressure. *Bulletin of JSME*, 27(229):1385-1392. https://doi.org/10.1299/jsme1958.27.1385

Zhang TT, Wang ZG, Huang W, et al., 2019. The overall layout of rocket-based combined-cycle engines: a review. *Journal of Zhejiang University-SCIENCE A (Applied Physics & Engineering)*, 20(3):163-183. https://doi.org/10.1631/jzus.A1800684

中文概要

题　目： 带有背景波系的隔离段内激波串自激振荡的实验研究与分析

目　的： 隔离段内存在背景波系时，激波串在自激振荡过程中会出现三种振荡模式，并表现出非对称结构。本文旨在研究背景波系是如何引起激波串的非对称结构以及背景波系对振荡特性的影响，并探究自激振荡的扰动来源。

创新点： 1. 从激波串结构和振荡特性两个方面揭示背景波系对激波串自激振荡的影响；2. 获得引起激波串自激振荡的扰动来源。

方　法： 1. 通过实验分析，结合激波极曲线，研究背景波系引起的压力间断对激波串结构的影响；2. 结合实验获得的激波串振荡特性以及数值模拟得到的壁面压力梯度，分析背景波系引起的压力梯度对自激振荡的影响；3. 通过对壁面压力进行相关性分析和相位分析，获得自激振荡扰动的来源。

结　论： 1. 背景波系引起的压力间断导致了激波串的非对称结构；2. 背景波系引起的壁面压力梯度影响激波串前缘的振荡范围和振荡强度；3. 在带有背景波系的隔离段内，引起自激振荡的扰动来源于前缘激波产生的分离区内。

关键词： 自激振荡；背景波系；非对称结构；扰动源